Research Article | Vol. 13, No. 1 / 1 Jan 2022 / Biomedical Optics Express 344
Biomedical Optics EXPRESS

Optical coherence tomography-guided confocal Raman microspectroscopy for rapid measurements in tissues

XIAOJING REN,[1,3] KAN LIN,[2,3] CHAO-MAO HSIEH,[1] LINBO LIU,[2] XIN GE,[2,4] AND QUAN LIU[1,5]

[1]School of Chemical and Biomedical Engineering, Nanyang Technological University, 70 Nanyang Drive, 637457, Singapore
[2]School of Electrical & Electronic Engineering, Nanyang Technological University, 50 Nanyang Ave, 639798, Singapore
[3]Equal contributors to paper.
[4]ustcgxtc@gmail.com
[5]liuquan@xmu.edu.cn

Abstract: We report a joint system with both confocal Raman spectroscopy (CRS) and optical coherence tomography (OCT) modules capable of quickly addressing the region of interest in a tissue for targeted Raman measurements from OCT. By using an electrically tunable lens in the Raman module, the focus of the module can be adjusted to address any specific depth indicated in an OCT image in a few milliseconds. We demonstrate the performance of the joint system in the depth dependent measurements of an *ex vivo* swine tissue and *in vivo* human skin. This system can be useful in measuring samples embedded with small targets, for example, to identify tumors in skin *in vivo* and assessment of tumor margins, in which OCT can be used to perform initial real-time screening with high throughput based on morphological features to identify suspicious targets then CRS is guided to address the targets in real time and fully characterize their biochemical fingerprints for confirmation.

© 2021 Optical Society of America under the terms of the OSA Open Access Publishing Agreement

1. Introduction

Raman spectroscopy (RS) is capable of revealing molecular composition with high specificity while optical coherence tomography (OCT) excels at imaging morphological microstructures with high spatial resolution. Hence the combination of RS and OCT can be used to obtain the molecular and morphological information of a given tissue region. The availability of molecular and morphological information in the same region can be critical in the fields of biology [1,2], pharmacology [3,4], and medical diagnostics [5–7], in order to evaluate drug distribution in tissues [8], the severity of burn wounds [9], and the boundary between healthy tissues and tumors [10,11]. Such a combination has been also demonstrated effective in the measurements of analytes in tissues [8], the characterization of anatomical structures in oral tissue and atherosclerotic plaque deposition [12,13] and the discrimination of different stages of bladder cancer [14].

Several sets of instrumentation that integrated RS and OCT have been reported as summarized in Table 1. The first such development can be traced back to 2008 by Patil et al. [15]. An RS module with 785-nm excitation source was combined with a time-domain OCT module. The RS module achieved an axial resolution of 600 μm and a lateral resolution of 75 μm. A pair of galvo mirrors was used to perform raster scanning in the lateral dimensions (x and y). As RS can only be performed along the central axis of the objective lens, a target region had to be moved to the center of the field of view of the objective lens using a translational stage after it was found in OCT images. In another joint system [16], an OCT model and a confocal Raman module was combined but without galvo mirrors therefore scanning had to be done by moving the sample

#441058 https://doi.org/10.1364/BOE.441058
Journal © 2022 Received 19 Aug 2021; revised 24 Oct 2021; accepted 6 Dec 2021; published 14 Dec 2021

Biomedical Optics EXPRESS

mounted on an automated x-y translational stage. The focal spot size and detection spot size in the RS were about 15 and 25 μm, respectively, which should be about the same order of magnitude as the lateral resolution of the system. There appeared no axial scanning. Different from these earlier systems with separate detection components, another joint system was developed in which the RS and the spectral-domain OCT modules shared the same spectrometer to save the cost and size [17]. In the RS module of this system, the axial and lateral resolutions were 425 μm and 15 μm. As the scanning mirrors and objective lens were arranged in a telecentric manner, RS could be performed along any A-scan in the OCT image but was not resolved in the axial dimension. In another dual-modal system, an OCT module with a central excitation wavelength of 1325 nm was combined with a typical RS to achieve an image depth of about 2.5 mm in pork tissues for the OCT system [18]. The Raman system has axial and lateral resolutions of 1000 μm and 100 μm, respectively. Chen et al. reported a wavelength modulated spatially offset RS module combined with a spectral domain OCT module. Benefiting from the wavelength modulation technique, the RS module contained minimal fluorescence background. By optimizing spatial offset between the excitation spot and collection spot, the RS modal was depth sensitive [19]. RS and OCT have also been integrated with an optoacoustics (OA) module to compensate for the limited penetration depth of OCT [20]. In this system, the RS used wide field illumination and the spot size matched the field of view of the OCT scanning lens. An iris was used to select an interesting region for Raman measurements. The same system but without the OA module was used for *in vivo* clinical melanoma skin cancer screening [21]. In another study, a back scattering spectroscopy was combined with RS and OCT with a fiber-optic probe as the shared sample arm to compensate for the slow RS measurements and improve diagnosis accuracy [22]. Patil et al. demonstrated a probe of 102.4 mm × 128 mm × 204.8 mm for skin cancer characterization [23] by integrating the previously reported Raman-OCT system [15]. Wang et al. designed a side-view handheld Raman-OCT optical probe with a size of 13 mm × 8 mm × 120 mm for real time tissue measurements in oral cavity [24]. Both the probes performed RS along the center axis of the objective lens with poor depth resolution. Klemes et al. introduced a probe that combined 632.8 nm confocal RS (CRS) and time-domain OCT systems [25]. In this probe, both the objectives of the RS and OCT systems were mounted on a rotary stage thus can scan along a common circular path, and the acquisition of Raman signals from a target depth was enabled by mechanically adjusting the Raman excitation focus.

The above survey of the past multi-modal RS/OCT systems suggests the following disadvantages. First, most joint systems have poor axial resolutions. In one exception [25], the sample arm was not shared between CRS and OCT so the switching from OCT imaging to Raman measurements (guided by OCT images) is performed by a rotary stage, which is not optimal in the measurements of dynamic samples and/or *in vivo* measurements. Second, axial scanning (if any) in the RS modules of these systems is achieved by moving the sample or the objective lens mounted on a translational stage, which can induce challenges in the stability and reproducibility of RS measurements.

To overcome these disadvantages, we developed a dual-modal system that integrated CRS and OCT with a shared arm, which was capable of rapidly addressing an arbitrary position for confocal Raman measurements in a tissue guided by OCT imaging. With the use of an electrically tunable lens (ETL), we were able to move the laser focus of the CRS module to an arbitrary location suggested by OCT imaging without any mechanical movement, which greatly sped up mode switching. The CRS module achieved a probing volume of about 1 mm (x) × 1 mm (y) × 0.87 mm (z), a spatial resolution of about 5 μm (x) × 5 μm (y) × 10 μm (z), and a spectral resolution of about 7 cm^{-1}. The coregistration error in target location between the CRS and OCT modules was 11.53 μm (x) × 13.86 μm (y) × 17.85 μm (z). The performance of the system was demonstrated in the measurements of an swine tissue *ex vivo* and human skin *in vivo*. Our system

Biomedical Optics EXPRESS

Table 1. Survey of joint Raman-OCT systems.

Ref.	Specifications (Raman)	Specifications (OCT)	Remarks
Patil, C.A., et al. [15]	Lateral res.: 75 µm Axial res.: 600 µm Laser: 785 nm	Lateral res.: 21 µm Axial res.: 25 µm Source: 1310 ± 30 nm	• This is the first reported joint RS and OCT system to our knowledge. • Sample arm was shared by Raman and OCT. • Lateral scanning was achieved by galvo mirrors. No axial scanning for RS.
Evans, J.W., et al. [16]	Lateral res.: 15 µm Axial res.: NM[a] Laser: 632.8 nm	Lateral res.: 18 µm Axial res.: 4.5 µm Source: 855 ± 35 nm	• Sample arm was shared by Raman and OCT. • Lateral scanning was achieved by moving the sample mounted on a translational stage. No axial scanning for RS.
Patil, C.A., et al. [17]	Lateral res.: 15 µm Axial res.: 425 µm Laser: 785 nm	Lateral res.: 18 µm Axial res.: 11 µm Source: 855 ± 20 nm	• RS and OCT shared the spectrometer to save cost and size and the sample arm. • Lateral scanning was achieved by galvo mirrors. No axial scanning for RS.
Egodage, K.D., et al. [18]	Lateral res.: 100 µm Axial res.: 1000 µm Laser: 785 nm	Lateral res.: 13 µm Axial res.: 10 µm Source: 1325 ± 100 nm	• Lateral scanning was achieved by galvo mirrors. No axial scanning for RS. • A probe head was developed to house the sample arm shared by both RS and OCT.
Chen, M., et al. [19]	Lateral res.: NM Axial res.: NM Laser: 785 nm	Lateral res.: NM Axial res.: NM Source: 850 ± 15 nm	• A wavelength modulated spatially offset RS module was combined with a spectral domain OCT. • Lateral scanning was achieved by galvo mirrors. Depth sensitivity was achieved by varying the spatial offset of the excitation fiber relative to the detection fiber. • Sample arm was shared by Raman and OCT.
Varkentin, A., et al. [20], Mazurenka, M., et al. [21]	Lateral res.: NM Axial res.: NM Laser: 532 nm, 7 ns, 20 Hz	Lateral res.: 13 µm Axial res.: 5.5 µm Source: 1310 nm	• A probe head housed the sample arm shared by RS and OCT [21]. The Optoacoustics (OA) module had a separate probe [20]. • Lateral scanning was achieved by galvo mirrors. No axial scanning for RS. • The Raman excitation spot matched the field of view of the OCT lens and an iris was used to select the region to be measured so the lateral resolution was expected to be poor.
Zakharov, V.P., et al. [22]	Lateral res.: NM Axial res.: NM Laser: 785 nm	Lateral res.: NM Axial res.: 3.5 µm Source: 840 ± 50 nm	• Backscattering spectroscopy, RS and OCT were integrated with a fiber probe as the shared sample arm. • No scanning included.
Patil, C.A., et al. [23]	Lateral res.: 44 µm Axial res.: 530 µm Laser: 785 nm	Lateral res.: 25 µm Axial res.: 14 µm Source: 1310 ± 30 nm	• The join system of RS and OCT in Ref. [15] was integrated with a probe for clinical applications.
Wang, J., et al. [24]	Lateral res.: 360 µm Axial res.: 300 µm Laser: 785 nm	Lateral res.: 12 µm Axial res.: 12 µm Source: 1325 ± 62.5 nm	• A sideview handheld RS-OCT probe was built. • The sample arms of RS and OCT were separate.
Klemes, J., et al. [25]	Lateral res.: NM Axial res.: 27.7 µm Laser: 632.8 nm	Lateral res.: 3.6 µm Axial res.: 4.3 µm Source: 880 ±31.65 nm	• Separate CRS and OCT were put together each with a different sample arm. • Two sample arms were mounted on one rotary stage to measure the same region in the lateral dimensions. • A linear stage was used for the axial adjustment of CRS focus.

[a]NM: Not mentioned.

Biomedical Optics EXPRESS

can be useful in the early detection of skin cancers, investigation of trans-follicular drug delivery, and the evaluation of cosmeceutical chemicals.

2. Instrument description

2.1. System setup

The schematic of the joint CRS-OCT setup is illustrated in Fig. 1 and a photo of the setup (primarily the Raman module and the shared sample arm) is shown in Fig. 2. The excitation light source in the Raman module was a 532-nm single-mode fiber-coupled laser (LCX-532S-300-CSB-PPF, Oxxius, Lannion, France). The excitation beam was collimated by a collimator (F220APC-532, Thorlabs, Newton, MA, USA) and then reflected by a dichroic mirror DM1 (Di03-R532-t1-25 × 36, Semrock, Rochester, NY, USA) and two mirrors towards ETL (EL-10-30-TC, Optotune, Dietikon, Switzerland). The focal length of ETL could be varied from 120 mm to 50 mm when the applied current was changed from 0 mA to 300 mA. The ETL is conjugate to the back focal plane of the objective lens (M Plan Apo NIR 20X, Mitutoyo Inc., Japan) through a 4f system composed of L2 and L1 (AC254-100-A-ML, Thorlabs, Newton, MA, USA), which enables any change in the light divergence immediately after the ETL due to its focal length varying to be relayed to the back aperture of the objective lens. As the ETL has a focal length of 120 mm even without current applied, L3 (LC1582-A, Thorlabs, Newton, MA, USA) with a focal length of –75 mm was added so that the Raman focal spot's location could be tuned to the OCT beam's focus when a certain current was applied. A pair of Galvo mirror (abbr. GM1, GM2, GVS012, Thorlabs, Newton, MA, USA) was used before the objective lens for lateral scanning.

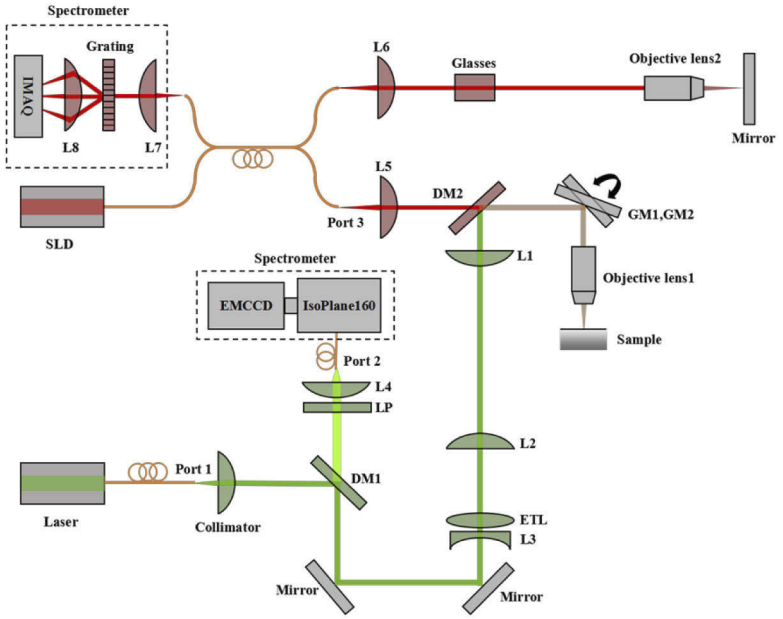

Fig. 1. Schematic of the experimental setup. DM1, DM2: Dichroic Mirror; ETL: Electrically Tunable Lens; L1, L2, L3, L4, L5, L6, L7, L8: Lens; GM1, GM2: Galvo Mirror; LP: Long Pass Filter; SLD: Super Luminescent Diode; EMCCD: Electron Multiplying Charge Coupled Device Camera; IMAQ: Image Acquisition System; Port 1 is for Raman excitation, Port 2 is for Raman collection, and Port3 is for OCT sampling arm.

Biomedical Optics EXPRESS

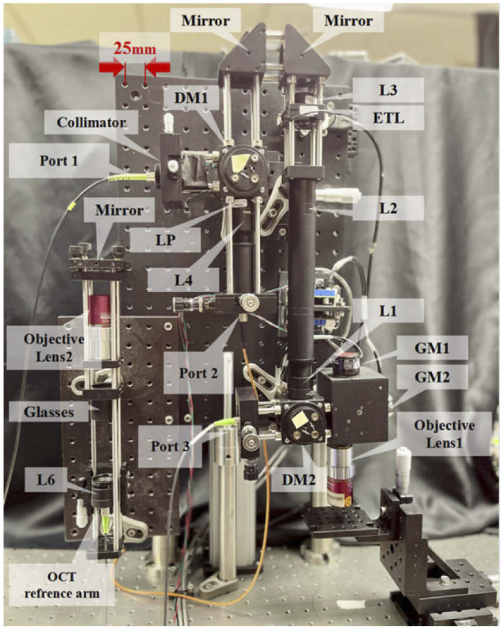

Fig. 2. Photo of the setup (primarily the Raman module and the shared sample arm).

The Raman light generated out of the sample was collected by the same objective lens and travelled backwards. After DM1, a long pass filter (abbr. LP, LP03-532RU-25, Semrock, Rochester, NY, USA) was used to remove laser light and an achromatic lens L4 (AC254-100-A-ML, Thorlabs, Newton, MA, USA) with a focal length of 100 mm was used to couple the Raman light into a fiber with a core diameter of 50 µm. The fiber also acted as a confocal pinhole, whose image size on the sample plane was about 4 µm, small enough to reject most out-of-focus light. The other end of the fiber was connected to a spectrometer equipped with a spectrograph (f/3.88, IsoPlane 160, Princeton Instrument, Trenton, NJ, USA) and an electron-multiplying charge coupled device (EMCCD) camera (ProEM:512B, Princeton Instrument, Trenton, NJ, USA).

The OCT imaging system used in this study has been previously reported except for the sample and reference arm optics [26]. In the sample arm, the light is collimated by an achromatic lens L5 (f = 4 mm) before passing through the dichroic and galvo mirrors. The reference arm is equipped with the same optics as the sample arm to balance the dispersion. The RS and the OCT modules shared the sample arm, which included GM1, GM2 and the objective lens. The light beams involved in two modules were combined using a dichroic mirror DM2 with an edge wavelength of 647.1 nm (Di03-R635-t1-25 × 36, Semrock, Rochester, NY, USA), which reflected the laser light (532 nm) and the Raman light (up to 647.1 nm) and passed light beams used in the OCT (wavelength range from 658.8 nm to 1200 nm).

2.2. Fabrication of phantoms

The sample used to characterize the scanning range of the CRS was a polystyrene plate, which was a fragment of a commercial cell culture dish (CLS430165, Corning, Tewksbury MA, USA). We fabricated the phantom for characterizing spatial resolutions of the CRS by dripping several microliter suspension of Nile red beads (F8819, FluoSphero, Waltham, USA) on a glass slide. To ensure that the beads were monodispersed, the stock suspension was diluted to achieve a volume concentration of 0.05 µL/mL. We dropped diluted bead suspension on a glass slide then dried it. The diameter of the beads was roughly 1 µm. To co-register the CRS and OCT systems, we

Biomedical Optics EXPRESS

used another type of Nile red beads with a diameter of 15 µm (FP-15056-2, Sphero, Chicago, IL, USA). The characterization of co-registration errors was performed on a layer of the beads on a glass slide, which was not similar to a tissue in scattering properties. This is only to serve as a reference for tissue measurements. The spatial resolution of the Raman module deteriorates significantly in a highly scattering medium just like other optical systems. As shown in Figs. 5(d) and 6(d), the maximum depth from which decent Raman spectra can be detected in the skin is around 300 micrometers.

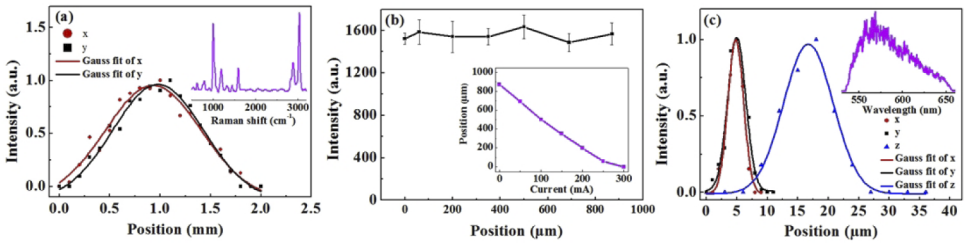

Fig. 3. (a) Intensity curve for estimating the field of view of the CRS module. The inset shows the spectrum of polystyrene. (b) Intensity curve for estimating the nominal sensing depth of the CRS module. The inset shows the relation between the current of the ETL and the focal position in the axial dimension. (c) The spatial resolutions of the RS module. The inset shows the spectrum of Nile red fluorescence beads.

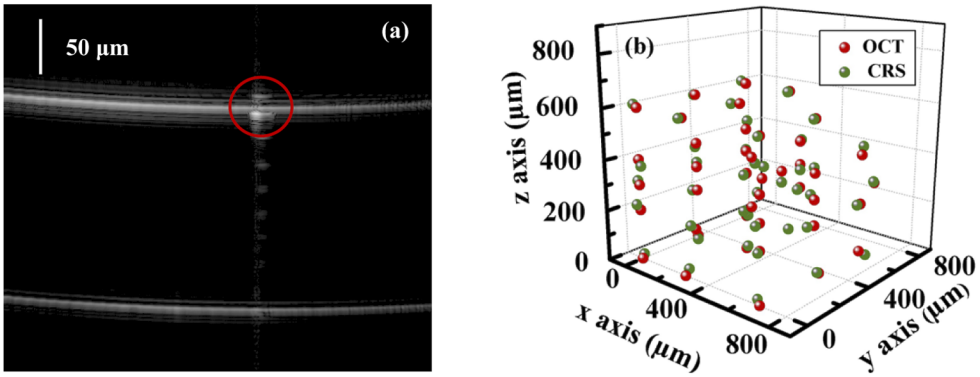

Fig. 4. (a) OCT image of a bead. (b) Location coregistration between the RS and OCT modules.

2.3. *Characterization of system specifications*

To measure the field of view of the CRS module, the laser focus was laterally scanned across the polystyrene plate and the Raman spectra were recorded once every 0.1 mm. The polynomial fitting technique was used to remove fluorescence background from raw Raman spectra throughout the paper. The detail of removing background from the raw spectra using the polynomial fitting technique was described in Refs. [27,28].The peak intensity of polystyrene at 1000 cm^{-1} extracted from the Raman spectra with background removed was plotted as a function of x and y displacement as shown in Fig. 3(a). It is observed that the intensity curves can be approximated as Gaussian functions of x and y. The full width at half maximum (FWHM) of each curve is estimated, which is treated as the field of view in the corresponding dimension. In this manner, the field of view was determined to be about 1 mm in both x and y dimensions. The nominal

Biomedical Optics EXPRESS

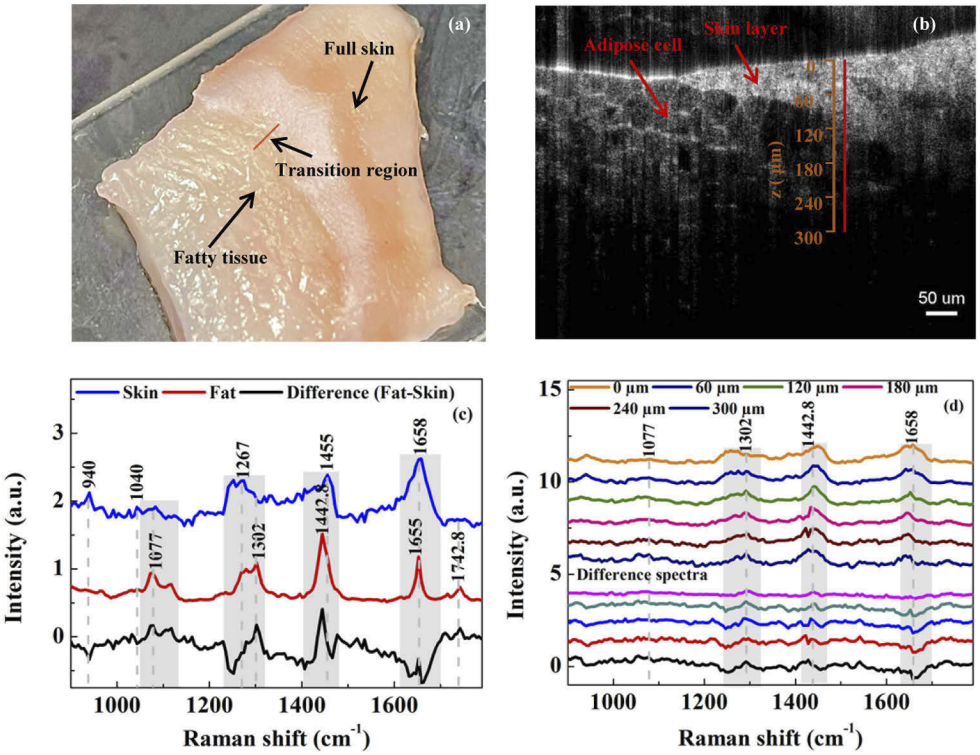

Fig. 5. (a) Photo of a diagonally cut swine tissue. (b) OCT image of the pork tissue. (c) Reference Raman spectra of skin layer, fatty tissue, and difference between skin and fat spectra in the pork tissue. (d) Depth dependent Raman spectra of the pork tissue measured along the red line in (c) with the guidance of the OCT image and the difference between the spectra at depths from 60 μm to 300 μm and that at a depth of 0 μm.

sensing depth range was determined by checking the intensity measured at 1000 cm^{-1} when the polystyrene plate was axially scanned. The intensity varied only slightly at different focuses, and the maximum sensing depth was found to be 870 μm as shown in Fig. 3(b), which was limited by the scanning range of the ETL. The inset of Fig. 3(b) shows the relation between the current of the ETL and the focal position in axial direction, which was measured by varying the current and then quantifying the depth change when moving the polystyrene sample axially on a translating stage to catch the laser focus and achieve the maximum Raman peak intensity. The spatial resolutions of the CRS module were measured by scanning the laser focus laterally and axially over a Nile red fluorescence bead with a diameter of 1 μm. The spectral intensity at 550 nm as shown in the inset of Fig. 3(c) was chosen to calculate the FWHM. The lateral and axial resolutions were found to be 3 μm and 10 μm, respectively, at the center of the field of view as shown in Fig. 3(c). In the entire sensing volume, the lateral resolution and axial resolution were 3.8 μm ± 0.4 μm and 13.5 μm ± 2.6 μm, respectively. The spectral resolution of the CRS module was estimated by measuring the spectrum of the single-mode Raman excitation laser that has a known line width of smaller than 1 MHz, which was found to be about 7 cm^{-1}.

For the OCT module, the axial resolution of OCT was measured to be 2.3 μm [29], and the FWHM transverse resolution is estimated to be 7.35 μm. The depth of focus, which is also known as confocal parameter, is estimated to be 300 μm. The scanning field of view of the OCT system was 1 mm by 1 mm. The sensitivity of the OCT imaging was measured to be 101.2 dB. The depth at which the 3-dB roll-off of OCT sensitivity occurs is 0.9 mm in air.

Biomedical Optics EXPRESS

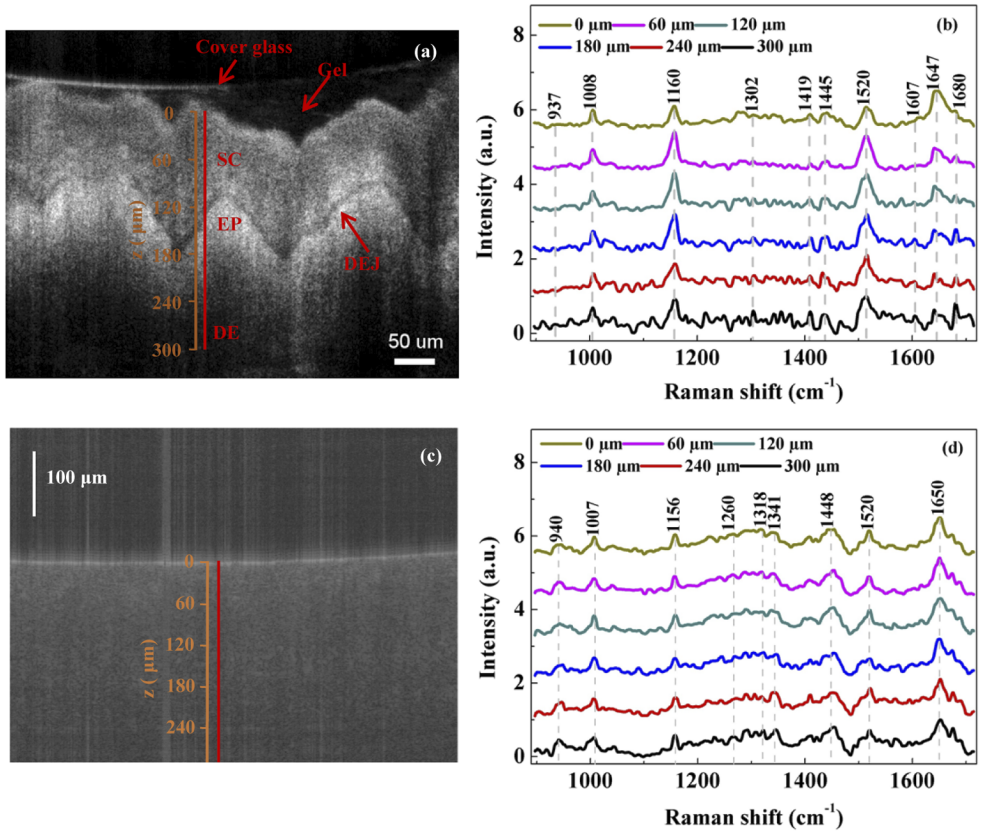

Fig. 6. (a) OCT image of *in vivo* human finger skin. SC: stratum corneum; EP: Epidermis; DEJ: Dermis epidermis junction; DE: Dermis. (b) Spectra of the *in vivo* human finger skin. (c) OCT image of *in vivo* human fingernail. (d) Spectra of the *in vivo* human fingernail.

2.4. Co-registration

We characterized the co-registration error of the two modules using Nile red fluorescence beads of 15 μm. These beads were large enough to be easily distinguished from air bubbles and impurities in an OCT image during co-registration. The co-registration error was qualified as the difference between the target location determined in the OCT image and the location of the laser focus of the Raman module that was programmed to match the target location. In an OCT image of the phantom shown in Fig. 4(a), a single bead was selected according to its shape and size as demarcated by the red circle. Then the excitation/detection focus of the Raman module was directed to the bead to measure the spectrum. In the measurement of spectrum, we used a translational stage to scan the bead laterally around the excitation/detection focus of the Raman module and tuned the applied current of the ETL finely to find the location that yields the maximum spectral intensity, which was considered as the true location of the bead. We repeated the above process at 43 positions in different regions across the entire field of view and depth range. The focuses of the two modules at these positions were shown in Fig. 4(b). The root mean square error (RMSE) of position co-registration was 11.53 μm in the x-axis, 13.86 μm in the y-axis, and 17.85 μm in the z-axis. As the co-registration error in the x-axis and the y-axis was close to the resolution limit of the translational stage, which is 10 μm, the actual errors may be smaller. The relatively larger co-registration error in the z-axis may be attributed to the focal shift of the ETL due to temperature fluctuation. The characterization of co-registration errors

Biomedical Optics EXPRESS

was performed on a layer of microbeads on a glass slide, which was not similar to the situation in tissues. This is only to serve as a reference for tissue measurements. The spatial resolution of the Raman module deteriorates significantly in a highly scattering medium just like other optical systems. As shown in Figs. 5 and 6, the maximum depth from which decent Raman spectra can be detected in the skin is around 300 µm. Table 2 summarizes the key parameters of the joint system.

Table 2. Summary of the system parameters.

	RS	OCT
Field of view	1 mm	1 mm
Effective imaging depth[a]	0.87 mm	1 mm
Lateral resolution	3 µm	7.35 µm
Axial resolution	10 µm	2.3 µm
Spectral resolution	7 cm^{-1}	Not applicable
Coregistration RMSE in x, y, and z	11.53 µm, 13.86 µm, 17.85 µm	

[a]Effective imaging depth refers to the imaging depth in an optically transparent sample for the CRS module and the penetration depth for the OCT.

2.5. Experimental parameters in tissue measurements

The laser power delivered onto samples in all Raman measurements was about 10 mW, which was far below the maximum permissible exposure (MPE) calculated according to American national standard for safe use of lasers (ANSI Z136.1). This study was approved by the Institutional Review Board (IRB) of Nanyang Technological University. The Raman signals from a depth of 200 µm and smaller were collected with an exposure time of 30 s and one time accumulation while the Raman signals below a depth of 200 µm were collected with 1-minute exposure time and one time accumulation. The light power on the sample from OCT was around 5 mW. OCT data was acquired at an A-line rate of 20 kHz. With 1024 A-line per frame, the OCT frame rate was 20 frames per second. Since OCT measures the optical path-length in vacuum, we have to reply on the knowledge of the refractive index in order to estimate the physical depth. In this study, we assume that the refractive index of both swine tissue and human skin is 1.38 according to the range of refractive index reported previously [1,2]. This approximation may introduce OCT measurement errors as the refractive index may vary with layer types and physiological states.

3. Results

3.1. Ex vivo skin tissue measurements

The performance of the dual-modal system was evaluated on a swine pork tissue sample taken from a piece of pork belly meat bought on a supermarket. We intended to include the boundary between skin layer and fatty tissue as the target measurement location. Since the thickness of porcine epidermis and dermis (~1.9 mm) [30] is larger than the penetration depth of 532 nm laser in tissues (smaller than 1 mm) [31], we cut the pork tissue diagonally across so that the boundary between the skin layer and fatty tissue was within the penetration depth of 532 nm laser as shown in Fig. 5(a). The full thickness of the skin could be observed on the right side of the sample while fatty tissue could be observed on the left side. Figure 5(b) was the OCT image of the tissue sample. Adipose cells were visible in the fatty tissue and the red line indicated the region where the Raman spectra were measured. From the OCT image, it was known that the target boundary was about 100 µm below the surface. We first obtained the reference skin layer and fatty tissue spectra by shifting the laser focus to the nearby superficial skin and fatty tissue as

Biomedical Optics EXPRESS

shown in Fig. 5(c). The spectra matched well with those reported in literature [32–34], such as the peaks of skin layer at 1040 cm^{-1} (assigned to collagen), 1267 cm^{-1} (assigned to Amide III), 1455 cm^{-1} (assigned to CH_2), 1658 cm^{-1} (assigned to Amide I) and the peaks of fatty tissue at 1077 cm^{-1} (assigned to C-C stretch in lipids), 1302 cm^{-1} (assigned to CH_2 twisting in lipids), 1442.8 cm^{-1} (assigned to CH_2 bending), 1655 cm^{-1} (assigned to C = C stretch), 1742.8 cm^{-1} (assigned to C = O ester in lipids). The differences in spectral features between the fatty tissue and skin layer were obvious. Peaks at 1077 cm^{-1} and 1302 cm^{-1} in the fatty tissue were stronger than those in the skin layer and the peak at 1442.8 cm^{-1} band was the strongest in the fatty tissue while comparable to that at 1658 cm^{-1} in the skin layer. Also shown in Fig. 5(c) is the difference spectrum obtained by subtracting the skin spectrum from the fat spectrum, it had both a valley and a peak in the band of 1250-1302 cm^{-1}, a peak at 1445 cm^{-1}, and a peak at 1655 cm^{-1}. Then we used the OCT image to guide Raman acquisition from the indicated region. The measured spectra and the difference spectra obtained by subtracting the spectrum at a depth of 0 μm from the spectra at depths of 60 μm to 300 μm are shown in Fig. 5(d). The features of spectra at a depth of 60 μm or above were similar to the skin layer reference spectrum in Fig. 5(c). For example, peaks at 1077 cm^{-1} and 1302 cm^{-1} were obscure. Moreover, peak intensities at 1442.8 cm^{-1} and 1658 cm^{-1} are comparable. In contrast, the features of spectra measured at depths from 120 μm to 300 μm are similar to the fatty tissue reference spectrum in Fig. 5(c). For example, the peaks at 1077 cm^{-1} and 1302 cm^{-1} gradually become more obvious with an increasing depth and the peak intensity at 1442.8 cm^{-1} is significantly higher than that at 1655 cm^{-1}. The features of the difference spectrum in Fig. 5(c) were also shown in the difference spectra for depths of 120 μm to 300 μm in Fig. 5(d). The qualitative agreement in spectral features between the measured Raman spectra and measurement depths from OCT images demonstrate the good coregistration between the CRS and OCT modules in the joint system.

3.2. *In vivo human skin measurements*

Finally, the performance of the dual-modal system was demonstrated in the *in vivo* measurements of the skin and nail in a finger of a volunteer. The OCT image of the skin region is shown in Fig. 6(a). The boundary between stratum corneum (SC) and epidermis (EP) was around 120 μm below the surface. Below the EP was the dermo-epidermal junction (DEJ) and dermis (DE). The Raman spectra are shown in Fig. 6(b). For a depth of 120 μm or above, which corresponds to SC, the features of Raman spectra looked very similar to each other, which included carotenoid peaks at 1008 cm^{-1} (assigned to the rocking motion of the methyl group), 1160 cm^{-1} and 1520 cm^{-1} (assigned to C = C bonds) [35], lipid peaks at 1419 cm^{-1} (assigned to CH_3 deformation) [36] and 1445 cm^{-1} (assigned to CH_2, CH_3 bending) [37], and protein peaks at 1647 cm^{-1} (assigned to C = O stretching Amide I) [36]. For the depths greater than 120 μm, additional peaks at 1302 cm^{-1} (assigned to C-H modes) [38], 1607 cm^{-1} (assigned to tyrosine) [39], 1680 cm^{-1} (assigned to Amide I) [39] progressively stand out as the depth increases. Moreover, the peak intensity ratio between 1647 cm^{-1} and 1445 cm^{-1} decreased compared to that in SC. The collagen peak at 937 cm^{-1} (assigned to C-C stretching of protein backbone) [38] at a depth of 300 μm suggested that it was in DE. The OCT image and Raman spectra of the fingernail are shown in Figs. 6(c) and 6(d), respectively. No obvious boundary was observed in the OCT image as expected. The features of the Raman spectra were mainly associated to keratin, such as peaks at 940 cm^{-1} (assigned to skeletal C-C stretch) [40], 1260 cm^{-1} (assigned to Amide III) [41], 1318 cm^{-1} and 1341 cm^{-1} (assigned to C-H bend) [40], and 1650 cm^{-1} (assigned to Amide I) [40]. Consistent with the trend in images, the spectral features of the fingernail changed little with depth.

4. Discussion

The axial tuning strategy using an ETL in the dual-modal system outperforms the conventional mechanical tuning strategy that involves a translational stage [15–19] in both speed and resolution.

Biomedical Optics EXPRESS

By varying the current applied to the ETL, the laser focus of the Raman module can be moved to an arbitrary location within the probing depth in about 5 milliseconds according to the specifications provided by the manufacturer of the ETL. This strategy can achieve a quite good tuning precision in the focal depth because the current applied to the ETL can be tuned finely. As a result, the axial resolution of our system is around 10 μm, which is better than any RS module previously achieved in similar dual-modal systems [15–25]. As no mechanical movement is required, this axial tuning strategy also ensures the stability and reproducibility of RS measurements. A laser wavelength of 532 nm can excite the spontaneous Raman signals of most biomolecules in human skin thus can be used to study various skin conditions including skin cancer [42]. In particular, carotenoid peaks obtained in our experiment are much stronger than those excited using near infrared light due to the fact that the laser wavelength of 532 nm falls in the resonance band of carotenoids [43]. In case that resonance enhancement dominates the Raman spectrum such that the general label-free characterization of the skin becomes difficult, one could consider changing the laser to a different visible wavelength to reduce resonance enhancement and highlight spontaneous Raman peaks without significantly modifying the entire setup.

To confirm that the cover glass and gel contributes insignificantly to the spectra in Fig. 6(b), we measured the Raman spectra of human skin, gel and coverslip separately under the same condition (result not shown). It can be seen that the spectral intensity of the skin is much greater than that of the gel and cover glass. This contrast would be more dramatic in actual measurements given that only the skin would be on focus while the gel and cover glass would be out of focus. Thus the influence of the gel and cover glass can be neglected.

The axial co-registration error of our system could be further reduced by mounting the ETL with a heat-conducting metal clamp and utilizing its built-in temperature sensor to stabilize the temperature. Another way that could potentially reduce the co-registration error is to use smaller beads for calibration, which may be able to minimize the uncertainty in Raman measurements. Here, beads with a size of 15 μm were used in this study to make a tradeoff between the CRS and OCT modules.

One considerable issue of the current system is that the weak Raman signal from a deep region inside a scattering tissue leads to a relatively long acquisition time. It takes 1 minute to acquire a Raman spectrum from a depth of greater than 200 μm in human skin. While this is inevitable in a highly scattering medium, the relatively low numerical aperture (NA) of the joint system further deteriorates this issue. As the objective lens is shared by the CRS and OCT, changing to an objective lens with a greater effective NA can increase the Raman signal but at the cost of the reduced effective imaging depth of the OCT module. In this case, the lens after the objective lens in the OCT module, i.e. L5 in Fig. 1, can be adjusted to alleviate this problem.

As illustrated in Fig. 2, the entire Raman module was installed on a breadboard with an overall size of 45 cm × 30 cm × 15 cm. The OCT module was fully enclosed in a box of a size of 55 cm x 55 cm x 30 cm. The original sample arm of the OCT module, which was an optical fiber, was coupled to the shared sampling optical path including the galvo mirrors and objective lens mounted on the Raman module. This compact and portable system is therefore flexible enough to adjust the orientation of the system's probe head, which makes it suitable for taking *in vivo* measurements from the skin. Given the capability of addressing an arbitrary voxel for skin measurements in real time and offering both morphological map and biochemical information at the same time, the dual-modal system has a great potential for diverse skin applications ranging from the early detection of skin cancer to biopharmaceutical investigations. For example, the system can be used to measure drug distribution in different skin parts during trans-follicular drug delivery. Another related field is cosmeceutical applications in which the distribution and outcome of cosmetic products when applied topically on the skin can be quantified with such a dual-modal system.

Biomedical Optics EXPRESS

5. Conclusion

We developed a joint CRS and OCT system that was capable of rapidly addressing an arbitrary location for confocal Raman measurements in a large tissue volume guided by OCT imaging. By using an ETL, the laser focus of the CRS module was able to shift to an arbitrary location suggested by OCT imaging without any mechanical movement. The coregistration error in target location between the CRS and OCT modules was 11.53 μm (x) × 13.86 μm × 17.85 μm (z). The system had a probing volume of 1 mm (x) × 1 mm (y) × 0.87 mm (z) and a spatial resolution set of 5 μm (x) × 5 μm (y) × 10 μm (z), and a spectral resolution of around 7 cm^{-1}. We demonstrated the performance of the system in the measurements of an *ex vivo* pork sample and *in vivo* human skin and fingernail. Our system can be useful in the early detection of skin cancer, investigation of trans-follicular drug delivery, and the evaluation of cosmeceutical products.

Funding. Ministry of Education - Singapore (MOE2017-T2-2-057, RG129/19, RT16/19); Agency for Science, Technology and Research (H17/01/a0/008, H17/01/a0/0F9).

Disclosures. The authors declare no conflicts of interest.

Data availability. Data underlying the results presented in this paper are not publicly available at this time but may be obtained from the authors upon reasonable request.

References

1. T. Kamali, B. Povazay, S. Kumar, Y. Silberberg, B. Hermann, R. Werkmeister, W. Drexler, and A. Unterhuber, "Hybrid single-source online Fourier transform coherent anti-Stokes Raman scattering/optical coherence tomography," Opt. Lett. **39**(19), 5709–5712 (2014).
2. C. Matthaus, S. Dochow, K. D. Egodage, B. F. Romeike, B. R. Brehm, and J. Popp, "Detection and characterization of early plaque formations by Raman probe spectroscopy and optical coherence tomography: an in vivo study on a rabbit model," J. Biomed. Opt. **23**(01), 1–6 (2018).
3. A. L. Presnell, O. Chuchuen, M. G. Simons, J. R. Maher, and D. F. Katz, "Full depth measurement of tenofovir transport in rectal mucosa using confocal Raman spectroscopy and optical coherence tomography," Drug Deliv. and Transl. Res. **8**(3), 843–852 (2018).
4. O. Chuchuen, J. R. Maher, M. H. Henderson, M. Desoto, L. C. Rohan, A. Wax, and D. F. Katz, "Label-free analysis of tenofovir delivery to vaginal tissue using co-registered confocal Raman spectroscopy and optical coherence tomography," PLoS ONE **12**(9), e0185633 (2017).
5. P. C. Ashok, B. B. Praveen, N. Bellini, A. Riches, K. Dholakia, and C. S. Herrington, "Multi-modal approach using Raman spectroscopy and optical coherence tomography for the discrimination of colonic adenocarcinoma from normal colon," Biomed. Opt. Express **4**(10), 2179–2186 (2013).
6. F. Placzek, E. Cordero Bautista, S. Kretschmer, L. M. Wurster, F. Knorr, G. Gonzalez-Cerdas, M. T. Erkkila, P. Stein, C. Ataman, G. G. Hermann, K. Mogensen, T. Hasselager, P. E. Andersen, H. Zappe, J. Popp, W. Drexler, R. A. Leitgeb, and I. W. Schie, "Morpho-molecular ex vivo detection and grading of non-muscle-invasive bladder cancer using forward imaging probe based multimodal optical coherence tomography and Raman spectroscopy," Analyst **145**(4), 1445–1456 (2020).
7. Y. Zhao, G. L. Monroy, S. You, R. L. Shelton, R. M. Nolan, H. Tu, E. J. Chaney, and S. A. Boppart, "Rapid diagnosis and differentiation of microbial pathogens in otitis media with a combined Raman spectroscopy and low-coherence interferometry probe: toward in vivo implementation," J. Biomed. Opt. **21**(10), 1 (2016).
8. J. R. Maher, O. Chuchuen, M. H. Henderson, S. Kim, M. T. Rinehart, A. D. Kashuba, A. Wax, and D. F. Katz, "Co-localized confocal Raman spectroscopy and optical coherence tomography (CRS-OCT) for depth-resolved analyte detection in tissue," Biomed. Opt. Express **6**(6), 2022–2035 (2015).
9. L. P. Rangaraju, G. Kunapuli, D. Every, O. D. Ayala, P. Ganapathy, and A. Mahadevan-Jansen, "Classification of burn injury using Raman spectroscopy and optical coherence tomography: An ex-vivo study on porcine skin," Burns **45**(3), 659–670 (2019).
10. V. V. Tuchin, K. V. Larin, M. J. Leahy, R. K. Wang, C.-H. Liu, J. Qi, J. Lu, S. Wang, C. Wu, W.-C. Shih, and K. V. Larin, "Improvement of tissue analysis and classification using optical coherence tomography combined with Raman spectroscopy," in *Dynamics and Fluctuations in Biomedical Photonics XI* (2014).
11. N. Sudheendran, J. Qi, E. D. Young, A. J. Lazar, D. C. Lev, R. E. Pollock, K. V. Larin, and W.-C. Shih, "Line-scan Raman microscopy complements optical coherence tomography for tumor boundary detection," Laser Phys. Lett. **11**(10), 105602 (2014).
12. J. Wang, W. Zheng, K. Lin, and Z. Huang, "Characterizing biochemical and morphological variations of clinically relevant anatomical locations of oral tissue in vivo with hybrid Raman spectroscopy and optical coherence tomography technique," J. Biophotonics **11**(3), e201700113 (2018).

Biomedical Optics EXPRESS

13. K. E. Kokila Egodage, C. M. Christian Matthus, S. D. Sebastian Dochow, I. W. S. Iwan, W. Schie, C. H. Carmen Hrdtner, I. H. Ingo Hilgendorf, and J. P. Jürgen Popp, "Combination of OCT and Raman spectroscopy for improved characterization of atherosclerotic plaque depositions," Chin. Opt. Lett. **15**(9), 090008 (2017).
14. D. Bovenkamp, R. Sentosa, E. Rank, M. Erkkilä, F. Placzek, J. Püls, W. Drexler, R. Leitgeb, N. Garstka, S. Shariat, C. Stiebing, I. Schie, J. Popp, M. Andreana, and A. Unterhuber, "Combination of high-resolution optical coherence tomography and raman spectroscopy for improved staging and grading in bladder cancer," Appl. Sci. **8**(12), 2371–2384 (2018).
15. C. A. Patil, N. Bosschaart, M. D. Keller, T. G. van Leeuwen, and A. Mahadevan-Jansen, "Combined Raman spectroscopy and optical coherence tomography device for tissue characterization," Opt. Lett. **33**(10), 1135–1137 (2008).
16. J. W. Evans, R. J. Zawadzki, R. Liu, J. W. Chan, S. M. Lane, and J. S. Werner, "Optical coherence tomography and Raman spectroscopy of the ex-vivo retina," J. Biophotonics **2**(6-7), 398–406 (2009).
17. C. A. Patil, J. Kalkman, D. J. Faber, J. S. Nyman, T. G. van Leeuwen, and A. Mahadevan-Jansen, "Integrated system for combined Raman spectroscopy-spectral domain optical coherence tomography," J. Biomed. Opt. **16**(1), 011007 (2011).
18. K. D. Egodage, S. Dochow, T. W. Bocklitz, O. Chernavskaia, C. Matthaeus, M. Schmitt, and J. Popp, "The combination of optical coherence tomography and Raman spectroscopy for tissue characterization," J. Biomed. Photonics Eng. **1**(2), 169–177 (2015).
19. M. Chen, J. Mas, L. H. Forbes, M. R. Andrews, and K. Dholakia, "Depth-resolved multimodal imaging: Wavelength modulated spatially offset Raman spectroscopy with optical coherence tomography," J. Biophotonics **11**(1), e201700129 (2018).
20. A. Varkentin, M. Mazurenka, E. Blumenrother, L. Behrendt, S. Emmert, U. Morgner, M. Meinhardt-Wollweber, M. Rahlves, and B. Roth, "Trimodal system for in vivo skin cancer screening with combined optical coherence tomography-Raman and colocalized optoacoustic measurements," J. Biophotonics **11**(6), e201700288 (2018).
21. M. Mazurenka, L. Behrendt, M. Meinhardt-Wollweber, U. Morgner, and B. Roth, "Development of a combined OCT-Raman probe for the prospective in vivo clinical melanoma skin cancer screening," Rev Sci Instrum **88**(10), 105103 (2017).
22. V. P. Zakharov, I. A. Bratchenko, D. N. Artemyev, O. O. Myakinin, D. V. Kornilin, S. V. Kozlov, and A. A. Moryatov, "Comparative analysis of combined spectral and optical tomography methods for detection of skin and lung cancers," J. Biomed. Opt. **20**(2), 025003 (2015).
23. C. A. Patil, H. Kirshnamoorthi, D. L. Ellis, T. G. van Leeuwen, and A. Mahadevan-Jansen, "A clinical instrument for combined raman spectroscopy-optical coherence tomography of skin cancers," Lasers Surg. Med. **43**(2), 143–151 (2011).
24. J. Wang, W. Zheng, K. Lin, and Z. Huang, "Development of a hybrid Raman spectroscopy and optical coherence tomography technique for real-time in vivo tissue measurements," Opt. Lett. **41**(13), 3045–3048 (2016).
25. J. Klemes, A. Kotzianova, M. Pokorny, P. Mojzes, J. Novak, L. Sukova, J. Demuth, J. Vesely, L. Sasek, and V. Velebny, "Non-invasive diagnostic system and its opto-mechanical probe for combining confocal Raman spectroscopy and optical coherence tomography," J. Biophotonics **10**(11), 1442–1449 (2017).
26. X. Ge, H. Tang, X. Wang, X. Liu, S. Chen, N. Wang, G. Ni, X. Yu, S. Chen, H. Liang, E. Bo, L. Wang, C. S. Braganza, C. Xu, S. M. Rowe, G. J. Tearney, and L. Liu, "Geometry-dependent spectroscopic contrast in deep tissues," iScience **19**, 965–975 (2019).
27. J. Zhao, H. Lui, D. I. McLean, and H. Zeng, "Automated autofluorescence background subtraction algorithm for biomedical Raman spectroscopy," Appl. Spectrosc. **61**(11), 1225–1232 (2007).
28. P. Mosier-Boss, S. Lieberman, and R. Newbery, "Fluorescence rejection in Raman spectroscopy by shifted-spectra, edge detection, and FFT filtering techniques," Appl. Spectrosc. **49**(5), 630–638 (1995).
29. L. Liu, J. A. Gardecki, S. K. Nadkarni, J. D. Toussaint, Y. Yagi, B. E. Bouma, and G. J. Tearney, "Imaging the subcellular structure of human coronary atherosclerosis using micro-optical coherence tomography," Nat Med **17**(8), 1010–1014 (2011).
30. U. Jacobi, M. Kaiser, R. Toll, S. Mangelsdorf, H. Audring, N. Otberg, W. Sterry, and J. Lademann, "Porcine ear skin: an in vitro model for human skin," Skin Res Technol **13**(1), 19–24 (2007).
31. G. H. Lee, H. Moon, H. Kim, G. H. Lee, W. Kwon, S. Yoo, D. Myung, S. H. Yun, Z. Bao, and S. K. Hahn, "Multifunctional materials for implantable and wearable photonic healthcare devices," Nat Rev Mater **5**(2), 149–165 (2020).
32. W. Liu, Y. H. Ong, X. J. Yu, J. Ju, C. M. Perlaki, L. B. Liu, and Q. Liu, "Snapshot depth sensitive Raman spectroscopy in layered tissues," Opt. Express **24**(25), 28312–28325 (2016).
33. J. W. Su, Q. Wang, Y. Tian, L. Madden, E. M. Ling Teo, D. L. Becker, and Q. Liu, "Depth-sensitive Raman spectroscopy for skin wound evaluation in rodents," Biomed Opt Express **10**(12), 6114–6128 (2019).
34. J. Mo, W. Zheng, and Z. Huang, "Fiber-optic Raman probe couples ball lens for depth-selected Raman measurements of epithelial tissue," Biomed Opt Express **1**(1), 17–30 (2010).
35. M. E. Darvin, W. Sterry, J. Lademann, and T. Vergou, "The role of carotenoids in human skin," Molecules **16**(12), 10491–10506 (2011).
36. L. Franzen and M. Windbergs, "Applications of Raman spectroscopy in skin research–From skin physiology and diagnosis up to risk assessment and dermal drug delivery," Adv Drug Deliv Rev **89**, 91–104 (2015).

Biomedical Optics EXPRESS

37. Y. Dancik, G. Sriram, B. Rout, Y. Zou, M. Bigliardi-Qi, and P. L. Bigliardi, "Physical and compositional analysis of differently cultured 3D human skin equivalents by confocal Raman spectroscopy," Analyst **143**(5), 1065–1076 (2018).
38. X. Feng, A. J. Moy, H. T. M. Nguyen, Y. Zhang, J. Zhang, M. C. Fox, K. R. Sebastian, J. S. Reichenberg, M. K. Markey, and J. W. Tunnell, "Raman biophysical markers in skin cancer diagnosis," J. Biomed. Opt. **23**(05), 1–10 (2018).
39. S. Tfaili, C. Gobinet, G. Josse, J. F. Angiboust, M. Manfait, and O. Piot, "Confocal Raman microspectroscopy for skin characterization: a comparative study between human skin and pig skin," Analyst **137**(16), 3673–3682 (2012).
40. E. Widjaja, G. H. Lim, and A. An, "A novel method for human gender classification using Raman spectroscopy of fingernail clippings," Analyst **133**(4), 493–498 (2008).
41. M. C. Caraher, A. Sophocleous, J. R. Beattie, O. O'Driscoll, N. M. Cummins, O. Brennan, F. J. O'Brien, S. H. Ralston, S. E. J. Bell, M. Towler, and A. I. Idris, "Raman spectroscopy predicts the link between claw keratin and bone collagen structure in a rodent model of oestrogen deficiency," Biochim Biophys Acta Mol Basis Dis **1864**(2), 398–406 (2018).
42. C. -H. Liu, B. Wu, L. A. Sordillo, S. Boydston-White, V. Sriramoju, C. Zhang, H. Beckman, L. Zhang, Z. Pei, L. Shi, and R. R. Alfano, "A pilot study for distinguishing basal cell carcinoma from normal human skin tissues using visible resonance Raman spectroscopy," JCMT **2019**(4), 1–14 (2019).
43. I. V. Ermakov and W. Gellermann, "Optical detection methods for carotenoids in human skin," Arch Biochem Biophys **572**, 101–111 (2015).